A Neural Network Model for Estimating the Particle Size Distribution of Dilute Latex from Multiangle Dynamic Light Scattering Measurements

Luis M. Gugliotta*, Georgina S. Stegmayer, Luis A. Clementi*, Verónica D. G. Gonzalez*, Roque J. Minari*, José R. Leiza***, Jorge R. Vega*, ****

(Received: 7 March 2008; in revised form: 11 October 2008; accepted: 10 March 2009)

DOI: 10.1002/ppsc.200800010

Abstract

The particle size distribution (PSD) of dilute latex was estimated through a general regression neural network (GRNN) that was supplied with PSD average diameters derived from multiangle dynamic light scattering (MDLS) measurements. The GRNN was trained with a large set of measurements that were simulated from unimodal normal-logarithmic distributions representing the PSDs of polystyrene (PS) latexes. The proposed method was first tested through three simulated examples involving different PSD shapes, widths, and diameter ranges. Then the GRNN was employed to estimate the PSD of two PS samples; a latex standard of narrow PSD and known nominal diameter, and a latex synthesized in our laboratory. Both samples were also characterized through independent techniques (capillary hydrodynamic fractionation, transmission electron microscopy, and disc centrifugation). For comparison, all examples were solved by numerical inversion of MDLS measurements through a Tikhonov regularization technique. The PSDs estimated by the GRNN gave more accurate results than those obtained through other conventional techniques. The proposed method is a simple, effective, and robust tool for characterizing unimodal PSDs.

Keywords: dynamic light scattering, latex, multiangle measurements, neural network, particle size distribution

1 Introduction

The particle size distribution (PSD) of a polymer colloid (or a latex) is an important characteristic that determines the end use properties (e.g., rheological, mechanical and physical properties) of the material when used as an adhesive, a coating or an ink. Also, it may influence the main physico-chemical mechanisms (absorption, desorption, and termination of free-radicals) that take place in some heterogeneous polymerization processes [1, 2]. Most the industrial latexes are obtained via emulsion polymerizations but can also be produced by miniemulsion, microemulsion, and dispersion polymerizations.

Transmission electron microscopy (TEM) is probably the most accurate technique for measuring narrow distributions of hard particles. Additionally, it can provide a detailed picture of particle shapes and morphology. However, TEM has several drawbacks [3–5]: i) it is only useful for measuring dry particles (i.e., isolated from their dispersion medium), ii) it is experimentally expensive, time-consuming, and difficult (especially when analyzing soft latexes and/or broad PSDs), iii) the electron

* Dr. L. M. Gugliotta, L. A. Clementi, Dr. V. D. G. Gonzalez, Dr. R. A. Minari, Dr. J. R. Vega (corresponding author), INTEC (CONICET and Universidad Nacional del Litoral), Güemes 3450, (3000) Santa Fe (Argentina).
E-mail: jvega@santafe-conicet.gov.ar

** Dr. G. S. Stegmayer, Dr. J. R. Vega, CIDISI (CONICET and UTN – Facultad Regional Santa Fe), Lavaise 610, (3000) Santa Fe (Argentina).

*** Dr. J. R. Leiza, POLYMAT and Dpto. Química Aplicada, University of Basque Country, Joxe Mari Korta zentroa, Tolosa Etorbidea 72, Donostia-San Sebastián (Spain).

beam can cause sample damage or size contraction, iv) for broad or multimodal PSDs thousands of particles must be counted, v) it tends to underestimate polydispersities and vi) automatic sizing can cause undesirable artifacts. Recently, however, a wet-STEM (scanning transmission electron microscopy) technique has been developed to analyze samples in water in a liquid state under transmission imaging conditions. Wet-STEM is basically an imaging mode in environmental scanning electron microscopy (ESEM) working under transmission conditions (STEM-in-SEM) [6, 7]. This technique can be used to determine the droplet size distribution of miniemulsions [8] but so far no results on the estimation of PSD of latexes have been published. Fractionation techniques, such as capillary hydrodynamic fractionation (CHDF), disc centrifugation (DC), field flow fractionation, and hydrodynamic chromatography are also employed for measuring PSDs. In particular, CHDF is a liquid chromatographic technique carried out in a capillary system fed with a highly accurate and reproducible flow of mobile phase (usually a solution of surfactants in deionized water). In CHDF, the particles are separated according to their sizes; large particles elute faster than smaller ones owing to the parabolic flow profile achieved inside the capillaries. A turbidity detector is typically used for determining the number of particles at each eluted fraction. Thus, CHDF is an indirect technique that requires a particle diameter calibration which is usually determined on the basis of narrow standards. Normally, CHDF produces broad PSDs as a consequence of peak broadening that mainly occurs in the capillary tube [9], but it is well suited to characterize multimodal PSDs [1, 10].

In DC, a hollow disc is filled with a spin-fluid, the sample is injected near the disc rotation axis, and the particles are separated due to the centrifugal force field. A turbidity detector is placed at the perimeter zone of the disc for evaluating the number of particles during the particle sedimentation process. On the basis of Stoke's law, particle diameters can be calculated directly from sedimentation times for known values of spin-fluid viscosity, disc rotational speed and differences between densities of particles and spin-fluid [11].

The so-called ensemble techniques are based on simultaneously measuring all particles in their media (without previous fractionation), and include optical techniques and acoustic-attenuation spectroscopy. The main optical methods for measuring particle diameters of dilute latexes are based on light scattering principles [12–14] and include dynamic light scattering (DLS), elastic light scattering (ELS), and turbidimetry (T). T measurements are usually carried out in a standard spectrophotometer. For DLS and ELS, the instruments basically consist of a monochromatic laser light that falls onto a dilute latex sample and a photometer placed at a given detection angle (with respect to the incident light), θ_r, that collects the light scattered by the particles over a small solid angle.

Mean diameters and PSDs of polymer latexes have been measured by T [3, 4], ELS [15, 16], and DLS [17–19]. The PSD is calculated by solving an 'ill-conditioned' inverse problem on the basis of a mathematical model describing the light scattering phenomena (e.g., Mie theory [12]). Unfortunately, single optical measurements give a small amount of information on PSD and consequently poor PSD resolution can be expected. The combination of two or more independent sets of measurements allows an increase in information content and can improve the quality of the PSD estimate. Some reported combinations are: T + ELS [20–22], multi-angle dynamic light scattering (MDLS) [23–27], and T + MDLS [28].

Let $f(D_i)$ be the discrete number PSD, where f represents the number-fraction of particles contained in the diameter interval $[D_i, D_{i+1}]$, with $i = 1, 2, ..., N$. All the D_i values are spaced at regular intervals ΔD along the diameter range $[D_{\min}, D_{\max}]$; thus, $D_i = D_{\min} + (I - 1)\,\Delta D$, with $\Delta D = (D_{\max} - D_{\min})/(N - 1)$.

In DLS, a devoted digital correlator allows the measurement of the second-order autocorrelation function of the light scattered at a given θ_r, $G^{(2)}_{\theta_r}(\tau_j)$, for different values of the time delay, τ_j. In MDLS, several measurements are taken at different θ_r ($r = 1, 2,..., R$). Such measurements are related to the (first-order and normalized) autocorrelation functions of the electric field, $g^{(1)}_{\theta_r}(\tau_j)$ through:

$$G^{(2)}_{\theta_r}(\tau_j) = G^{(2)}_{\infty,\theta_r}\left[1+\beta\left(g^{(1)}_{\theta_r}(\tau_j)\right)^2\right]; j = 1, ..., M\,; r = 1, ..., R, \quad (1a)$$

where $G^{(2)}_{\infty,\theta_r}$ is the measured baseline, β (<1) is an instrumental parameter, and M is the number of points of the autocorrelation functions (limited by the number of available correlator channels). For a given angle, $g^{(1)}_{\theta_r}(\tau_j)$ is related to $f(D_i)$ as follows [27]:

$$g^{(1)}_{\theta_r}(\tau_j) = k_{\theta_r}\sum_{i=1}^{N} e^{-\frac{\Gamma_0(\theta_r)\tau_j}{D_i}} C_I(\theta_r, D_i) f(D_i);$$

$$i = 1, ..., N\,; j = 1, ..., M, \quad (1b)$$

where k_{θ_r} are (a priori unknown) constants, at each θ_r; C_I is the fraction of light intensity scattered by a particle of diameter D_i at θ_r, at given values of light polarization and laser wavelength, that can be calculated through Mie scattering theory [12]. The parameter $\Gamma_0(\theta_r)$ is calculated by:

$$\Gamma_0(\theta_r) = \frac{16\pi}{3}\left(\frac{n_m}{\lambda}\right)^2 \frac{k_B T}{\eta}\sin^2(\theta_r/2)\,; \quad r = 1, ..., R, \quad (1c)$$

where λ is the in vacuo wavelength of the incident laser light, n_m is the refractive index of the non-absorbing medium, k_B (= $1.38 \cdot 10^{-23}$ kg m^2 s^{-2} K^{-1}) is the Boltzmann constant, T is the absolute temperature and η is the medium viscosity at T.

At a given θ_r, a fast and reliable estimate of an average diameter of the PSD can be obtained through the cumulant method [29]. Alternatively, the complete PSD, $f(D_i)$, can be estimated by inverting Eqs. (1b and c) on the basis of either single-angle DLS or MDLS measurements. Such an inverse problem is normally 'ill-conditioned'; i.e., small errors in measurement (for example, small perturbations due to the measurement noise) can give large changes in the estimation of $f(D_i)$. Moreover, the difficulty of the inverse problem increases as the distribution becomes narrower.

Regularization methods aim at improving the numerical inversion by including adjustable parameters, a priori knowledge of the solution, or some smoothness conditions [30–32]. While a strong regularization produces an excessively smoothened and wide PSD, a weak regularization normally creates oscillatory PSD estimates and therefore a trade-off solution must be selected. Particularly, the nonnegative-constraint Tikhonov regularization method [30] involves a single adjustment parameter, which can automatically be determined through the so-called L-curve method [33]. The constrained regularization method proposed by Provencher [34] is often used for inverting ill-conditioned integral linear equations. The method was originally implemented in FORTRAN [35] and it is available in the public domain. Other similar regularization tools (coded as a MATLAB package) for inverting discrete ill-posed problems are also available [36].

For data treatment of MDLS measurements, different approaches have been proposed to estimate the PSD [23–27]. For example, the inverse problem of Eq. (1b) was solved by calculating in a single operation the weighting coefficients k_{θ_r} and the PSD [25,26]. Also, a sequential method was proposed [27] that first estimated the weighting coefficients on the basis of the autocorrelation functions and then estimated the PSD by direct inversion of Eq. (1b).

In general, the estimation of a narrow PSD by DLS is difficult. Small PSD polydispersities can be detected by analyzing the angular variation of the effective diffusion coefficient, which can be estimated from the slopes of the autocorrelation functions measured by MDLS [37]. The method was refined by combining MDLS and ELS measurements [38]. The required experimental information included the angular variation of the intensity form factor (derived from the ELS measurement) and the apparent radius (derived from the DLS measurement). These measurements were simulated on the basis of Mie theory for a large set of normal-logarithmic, Gaussian and Weibull PSDs. The final estimate was selected as the PSD that produced the best fit for the experimental data. The method was recently validated on the basis of independent measurements by scanning electron microscopy [5].

Several neural network (NN) methods have also been applied for solving inverse problems in light scattering systems to estimate shape, size, and orientation of polymer particles [39–44]. For instance, radial basis function NNs proved adequate for simultaneously estimating the average radius and the particle refractive index in a system with homogeneous spheres on the basis of ELS measurements [39]. Simulated and experimental results showed the ability of NNs for estimating the parameters of a log-normal PSD (i.e, the mean diameter and the standard deviation) from turbidity measurements [40]. An important limitation of the method is that the particle refractive index must be accurately known, or alternatively, well-characterized PSDs should be used to experimentally train the NN [40]. Finally, multi-level NNs with linear activation functions were used to estimate the average size, the aspect ratio, and the orientation of prolate spheroidal particles with equivalent radii in the range $3.00 \cdot 10^{-7}$–$1.50 \cdot 10^{-6}$ m (300–1500 nm) [42]. Such methods were further extended to determine the same parameters in a binary mixture of cylindrical and spheroidal particles [43]. As far as the authors are aware, no NN-based method has yet been published for estimating the complete PSD from MDLS measurements.

In this work, a novel method that employs the average diameters determined in MDLS measurements is proposed for estimating the PSD of polymer colloids. The estimation model was implemented through a NN that was trained with a large set of typical asymmetric PSDs and their corresponding simulated measurements. The proposed method was then evaluated through both, synthetic and experimental examples. All the estimated PSDs were compared with independent estimations obtained through a classical inversion method of MDLS measurements. The latexes used in the experimental examples were also characterized by TEM, CHDF and DC.

2 The Proposed Method

For solving the MDLS problem, we propose replacing Eqs. (1b and c) with a nonlinear expression that allows the evaluation of the average diameter typically calculated in a MDLS measurement at each θ_r, $\bar{D}_{DLS}(\theta_r)$, i.e., [27]:

$$\bar{D}_{DLS}(\theta_r) = \frac{\sum_{i=1}^{N} C_I(\theta_r, D_i) f(D_i)}{\sum_{i=1}^{N} \frac{C_I(\theta_r, D_i) f(D_i)}{D_i}}; \quad r = 1, ..., R; \quad i = 1, ..., N. \tag{2}$$

Clearly, each $\bar{D}_{\mathrm{DLS}}(\theta_r)$ could be calculated from Eq. (2) only when the PSD is known. In practice, however, $\bar{D}_{\mathrm{DLS}}(\theta_r)$ could be directly computed from $g^{(1)}_{\theta_r}(\tau)$ (in turn derived from $G^{(2)}_{\theta_r}(\tau_j)$ through Eq. (1a)), by means of the cumulant method [29] as is schematically represented in the left side of Figure 1. In general, $\bar{D}_{\mathrm{DLS}}(\theta_r)$ varies with θ_r, except under the following rather particular conditions: i) for a monodisperse PSD (all particles of identical diameter, D_0) where Eq. (2) yields $\bar{D}_{\mathrm{DLS}}(\theta_r) = D_0$ and ii) for (small) particles in the so-called Rayleigh region where $C_I(\theta_r, D_i) \propto D_i^6$ and Eq. (2) yields a mean diameter independent of θ_r.

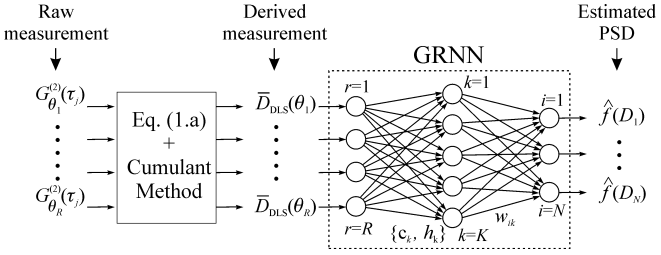

Fig. 1: Estimation of a latex PSD from MDLS measurements and on the basis of a GRNN model. Schematic representation of the proposed method.

To estimate the PSD from Eq. (2) on the basis of the $\bar{D}_{\mathrm{DLS}}(\theta_r)$ 'measurements', an 'ill-conditioned' non-linear inverse problem must be solved. As an alternative, we propose the estimation of $f(D_i)$ through a NN-based model, and to this effect, a general regression neural network (GRNN) was employed. In general, GRNNs have proven useful for function approximations [45].

A brief explanation of the employed NN is given here (see right side of Figure 1). The NN has 'R' input variables, the average mean diameters, $\bar{D}_{\mathrm{DLS}}(\theta_r)$ derived from the raw measurements, $G^{(2)}_{\theta_r}(\tau_j)$ and 'N' output variables, the estimated ordinates $\hat{f}(D_i)$ of the required PSD, $f(D_i)$. The information can be arranged in two column vectors: the input vector $\mathbf{D_{DLS}} = [\bar{D}_{\mathrm{DLS}}(\theta_1), \bar{D}_{\mathrm{DLS}}(\theta_2),..., \bar{D}_{\mathrm{DLS}}(\theta_R)]^{\mathrm{T}}$, and its corresponding output (or target) vector $\hat{\mathbf{f}} = [\hat{f}(D_1), \hat{f}(D_2), ..., \hat{f}(D_N)]^{\mathrm{T}}$, where the superscript T indicates the transposed vector. A NN model can be useful for describing the input/output behavior of a system if it is trained with a supervised learning algorithm using the knowledge of P particular input/output vector pairs, $\{\mathbf{D}^p_{\mathbf{DLS}}, \mathbf{f}^p\}$, $p = 1, ..., P$, as a priori information during the NN training.

A radial basis function (RBF) NN has a simple architecture with only one hidden layer with K neurons (or radial basis units) [46]. The most common shape of these neuron activation functions is Gaussian that exhibits a radial symmetry around its center, c_k ($R \times 1$), with $k = 1, ..., K$. A RBF NN model relates the output of the k-th hidden neuron, h_k, with the input vector $\mathbf{D_{DLS}}$, through:

$$h_k = e^{-\frac{\left\|\mathbf{D_{DLS}} - \mathbf{c}_k\right\|^2}{2\sigma^2_{s,k}}}; \quad k = 1, ..., K, \tag{3a}$$

where the scalar magnitude $\|\mathbf{D_{DLS}} - \mathbf{c}_k\|$ represents the Euclidean distance between the vectors $\mathbf{D_{DLS}}$ ($R \times 1$) and c_k ($R \times 1$), and $\sigma_{s,k}$ is the smoothing parameter (or 'spread') associated with the k-th hidden neuron. The normalized i-th output of the RBF network, $\hat{f}(D_i)$, is simply a weighted linear combination of the hidden neuron outputs and is obtained as follows:

$$\hat{f}(D_i) = \frac{\sum_k w_{ik} h_k}{\sum_k h_k}; \quad i = 1, ..., N, \tag{3b}$$

where w_{ik} are the hidden-to-output weight factors.

The GRNN is a particular case of a RBF network [47], where each $\mathbf{D}^p_{\mathbf{DLS}}$ is adopted as the center of a neuron, i.e., $\mathbf{D}^k_{\mathbf{DLS}} = c_k$, and therefore the number of hidden neurons in the GRNN coincides with the number of pairs $\{\mathbf{D}^p_{\mathbf{DLS}}, \mathbf{f}^p\}$ that is used during the training stage (i.e., $k = p$ and $K = P$). Training of a GRNN is straightforward. In fact the coefficients w_{ik} of the k-th neuron are directly set as its corresponding target values. The GRNN works as a one pass learning algorithm with a highly parallel structure and even with sparse data in a multidimensional measurement space, it provides smooth transitions from one observed value to another [45].

A GRNN network will tend to respond with the target vector $\mathbf{f}^k$ associated with the nearest design input vector $\mathbf{D}^k_{\mathbf{DLS}}$ seen during training. In general, for a particular input $\mathbf{D_{DLS}}$, the GRNN output $\hat{\mathbf{f}}$ is simply a weighted average of the target values $\mathbf{f}^k$ corresponding to those $\mathbf{D}^k_{\mathbf{DLS}}$ that are close to the given $\mathbf{D_{DLS}}$. The $\sigma_{s,k}$ spreads can be empirically determined, although often a single value is used for all the radial units. A small $\sigma_{s,k}$ directs the neuron to be highly selective, and its output will be meaningful only for an input $\mathbf{D_{DLS}}$ close to c_k. In contrast, a large $\sigma_{s,k}$ indicates that the k-th neuron output will be influenced by different distant $\mathbf{D_{DLS}}$ inputs. Several neurons will respond to an input vector and therefore the NN will have a greater smoothing ability [47]. For instance, for a given neuron k, if $\mathbf{D_{DLS}} \equiv c_k$, then $\|\mathbf{D_{DLS}} - \mathbf{c}_k\| = 0$, $h_k = 1$ (whereas $h_q = 0 \ \forall \ q \neq k$), and $\hat{f}(D_i) \equiv w_{ik} \equiv f(D_i)$. In contrast, if $\|\mathbf{D_{DLS}} - \mathbf{c}_k\| = 1.177 \times \sigma_{s,k}$, then $h_k = 0.5$, and therefore more than one hidden unit will contribute to the estimated $\hat{f}(D_i)$.

3 Training of the NN Based Model

The NN was trained on the basis of simulated data given by a set of discrete PSDs and their corresponding 'syn-

thetic measurements' obtained from Eq. (2). The D_i and θ_r axes were assumed to be fixed and therefore only the ordinates of $f(D_i)$ and $\bar{D}_{\mathrm{DLS}}(\theta_r)$ were processed by the NN. Each a priori known $f(D_i)$ was placed in the diameter range $5.00 \cdot 10^{-8}$–$1.10 \cdot 10^{-6}$ m (i.e., 50–1100 nm), at regular intervals $\Delta D = 5.0 \cdot 10^{-9}$ m (i.e., 5 nm). In all cases, the 'measurements' were taken in the angle range of 20°–140° at regular intervals of 10°, and they were obtained from Eq. (2), with the C_I values calculated through Mie theory for polystyrene (PS) particles. Thus, the NN inputs, $\bar{D}_{\mathrm{DLS}}(\theta_r)$, were represented by $R = 13$ values, and the NN outputs, $f(D_i)$, were represented by $N = 211$ values.

The PSD was restricted to unimodal, fixed log-normal shape, given by:

$$f(D_i) = \frac{\Delta D}{D_i \sigma_{\mathrm{L}} \sqrt{2\pi}} \exp\left[- \frac{\left[\ln(D_i/\bar{D}_g)\right]^2}{2\sigma_{\mathrm{L}}^2} \right];\ i = 1, ..., N, \quad (4)$$

where D_i (i = 1, 2, ..., 211) represents the discrete diameter; $\bar{D}_g$ is the geometric mean diameter, and σ_{L} is the standard deviation of the PSD.

For generating the training set, $\bar{D}_g$ was varied in the range of $1.00 \cdot 10^{-7}$–$1.00 \cdot 10^{-6}$ m (100–1000 nm), at regular intervals of $5.0 \cdot 10^{-9}$ m (5 nm). For each $\bar{D}_g$, 20 distributions were generated with standard deviations in the range of 0.01–0.20 at regular intervals of 0.01. Hence, 181 different $\bar{D}_g$ values were considered, with 20 PSDs of different standard deviations for each geometric mean, thus yielding a total of $P = 3620$ training patterns. All patterns were normalized to fall in the range of 0 to 1. The network learned the training data perfectly, with an approximate root mean square error of 10^{-5}. Note that at high $\bar{D}_g$, the broader PSDs did not decay towards zero at the upper limit of D_i ($D_{\max} = 1.10 \cdot 10^{-6}$ m (1100 nm)). For this reason, broad PSDs exhibiting large mean diameters should not be analyzed with this NN. In such a case, new NN training would be necessary in a proper diameter range.

4 NN Based Model Validation with Simulated Examples

The NN was first validated through simulated or 'synthetic' examples, because in these cases the solutions are 'a priori' known, and therefore the NN performance can be quantified. Three PSDs corresponding to a hypothetical PS latex were considered that involve different shapes and diameter ranges. The first PSD, $f_1(D_i)$, exhibited an asymmetric log-normal distribution as given by Eq. (4), with $\bar{D}_g = 2.03 \cdot 10^{-7}$ m (203 nm) and $\sigma_{\mathrm{L}} = 0.115$. The second PSD, $f_2(D_i)$ was assumed as an asymmetric exponentially-modified Gaussian (EMG) distribution, obtained by convoluting a Gaussian distribution of mean diameter $\bar{D}_{\mathrm{G}} = 3.40 \times 10^{-8}$ m (340 nm) and standard deviation $\sigma_{\mathrm{G}} = 1.0 \cdot 10$ m (10 nm) with a decreasing exponential function of decay constant $\tau = 2.0 \cdot 10^{-8}$ m (20 nm) as follows:

$$f_2(D_i) = \frac{\Delta D}{\sqrt{2\pi}\sigma_{\mathrm{G}}} \exp\left[- \frac{(D_i - \bar{D}_{\mathrm{G}})^2}{2\sigma_{\mathrm{G}}^2} \right] * \frac{\exp(-D_i/\tau)}{\tau/\Delta D};\ i = 1, ..., N, \quad (5)$$

where the symbol "*" represented the convolution product. The third PSD, $f_3(D_i)$, exhibited a symmetric Gaussian distribution of mean diameter $\bar{D}_{\mathrm{G}} = 4.50 \cdot 10^{-7}$ m (450 nm) and standard deviation $\sigma_{\mathrm{G}} = 4.25 \cdot 10^{-8}$ m (42.5 nm).

The three selected PSDs are represented in Figures 2a, 3a, and 4a by dashed lines. Notice that $f_1(D_i)$ had the same shape used for training the NN and for this reason it was useful for evaluating the model interpolation ability. In contrast, $f_2(D_i)$ exhibited a higher asymmetry than a log-normal distribution while $f_3(D_i)$ was symmetric and they were selected to evaluate the ability of the NN for estimating PSDs with different shapes than those used during the training stage.

For simulating the MDLS measurements, it was assumed that the light scattering photometer was fitted with a vertically polarized He-Ne laser. At the laser wavelength $\lambda = 6.328 \cdot 10^{-7}$ m (632.8 nm), the refractive indexes are: $n_p = 1.5729$ for the PS particles, and $n_m = 1.3319$ for the dispersion medium (pure water) [48, 49]. These optical parameters were used to evaluate $C_I(\theta_r, D_i)$ through Mie theory [12], and were required to simulate the $\bar{D}_{\mathrm{DLS}}(\theta_r)$ 'measurements' through Eq. (2). Figure 5 shows the $C_I(\theta_r, D_i)$ coefficients in a wide range of diameters, and for several arbitrarily selected θ_r's. At

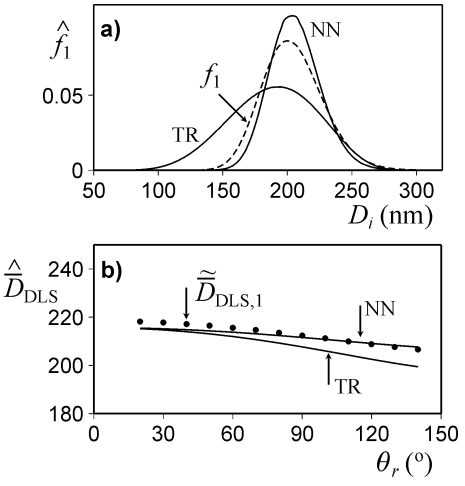

Fig. 2: Simulated example: estimation of a log-normal PSD, $f_1(D_i)$. a) The 'true' PSD and its estimation through the NN and TR techniques. b) The noisy average diameters, $\bar{D}_{\mathrm{DLS},1}(\theta_r)$, calculated from the MDLS measurements (dots), and their simulated values obtained from the estimated PSDs (continuous lines).

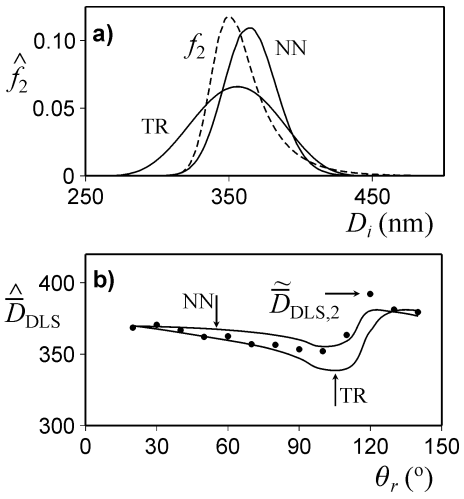

Fig. 3: Simulated example: estimation of an EMG PSD, $f_2(D_i)$. a) The 'true' PSD and its estimation through NN and TR techniques. b) The noisy average diameters, $\tilde{\bar{D}}_{DLS,2}(\theta_r)$, calculated from the MDLS measurements (dots), and their simulated values obtained from the estimated PSDs (continuous lines).

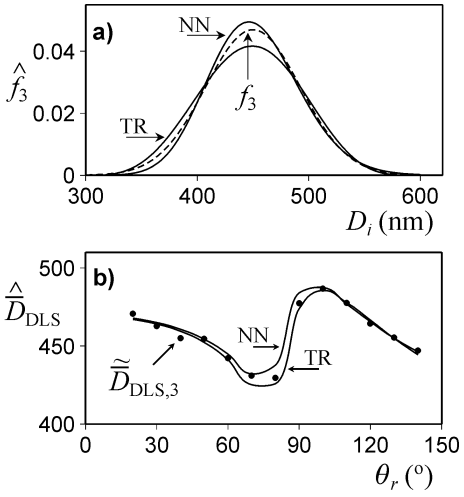

Fig. 4: Simulated example: estimation of a Gaussian PSD, $f_3(D_i)$. a) The 'true' PSD and its estimation through the NN and TR techniques. b) The noisy average diameters, $\tilde{\bar{D}}_{DLS,3}(\theta_r)$, calculated from the MDLS measurements (dots), and their simulated values obtained from the estimated PSDs (continuous lines).

low D_i (<$6.0 \cdot 10^{-8}$ m (60 nm)), any particle scatters the same amount of light at all θ_r's (according to the Rayleigh scattering model), and therefore the $C_I(\theta_r, D_i)$ coefficients were almost independent of θ_r. For larger D_i, the light scattered by a particle depends on θ_r and the resulting variations in $C_I(\theta_r, D_i)$ suggested that a set of measurements taken at several θ_r's would be able to capture more information on particle size than a single measurement taken at a given θ_r. In contrast, for $D_i < 6.0 \cdot 10^{-8}$ m (60 nm), multi-angle measurements would not incorporate additional information on the particle sizes.

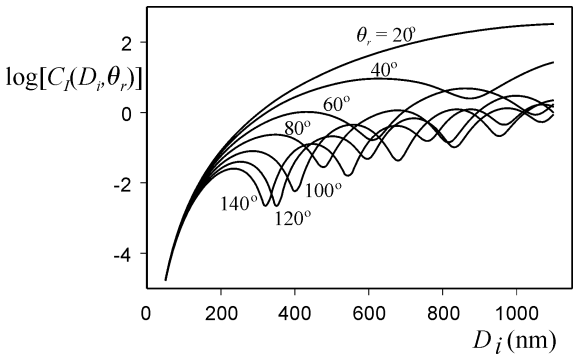

Fig. 5: Mie coefficients, $C_I(\theta_r,D_i)$, for 7 different θ_r's between 20° and 140°. In the Rayleigh region ($D_i < 6.0 \times 10^{-8}$ m (60 nm)) all curves are practically coincident, and therefore no additional information can be obtained by measuring at different θ_r's.

In order to simulate 'synthetic' noisy measurements of the mean diameters, $\tilde{\bar{D}}_{DLS}(\theta_r)$, similar to those found in the experimental work, the simulated noise free measurements, $\bar{D}_{DLS}(\theta_r)$, were contaminated with additive Gaussian noises, as follows:

$$\tilde{\bar{D}}_{DLS}(\theta_r) = \bar{D}_{DLS}(\theta_r) + A\bar{\bar{D}}_{DLS}\varepsilon(\theta_r), \tag{6}$$

where $\varepsilon(\theta_r)$ is a Gaussian random sequence of mean zero and variance one, $\bar{\bar{D}}_{DLS}$ is the mean of $\bar{D}_{DLS}(\theta_r)$ and A (= 0.0064) is a constant that was adjusted to reproduce typical variations of $\tilde{\bar{D}}_{DLS}(\theta_r)$ observed when the cumulant method [29] was used to estimate $\bar{D}_{DLS}(\theta_r)$ from measurements carried out in commercial equipment. Figures 2b, 3b, and 4b (dots) show the evolution of $\tilde{\bar{D}}_{DLS}(\theta_r)$. From $\bar{D}_{DLS}(\theta_r)$ the trained NN predicted the PSDs indicated in Figures 2a, 3a, and 4a.

The autocorrelation measurements were also processed by means of a MDLS technique [24, 27] and the inverse problem was solved through a nonnegative-constraint Tikhonov regularization (TR) method, with automatic selection of the regularization parameter according to the L-curve method [30, 33, 36]. The obtained PSD estimates are also represented in Figures 2a, 3a, and 4a. The estimated mean DLS diameters can be calculated by introducing the predicted distributions into Eq. (2), thus producing the estimated mean diameters $\hat{\bar{D}}_{DLS,1}(\theta_r)$, $\hat{\bar{D}}_{DLS,2}(\theta_r)$, and $\hat{\bar{D}}_{DLS,3}(\theta_r)$, that are also represented in Figures 2b, 3b, and 4b.

The quality of the estimations was evaluated through the following performance indexes:

$$J_f = \left(\frac{\sum_{i=1}^{N} \left[f(D_i) - \hat{f}(D_i) \right]^2}{\sum_{i=1}^{N} [f(D_i)]^2} \right)^{0.5} \tag{7a}$$

$$E_D = \frac{\bar{D}_n - \hat{\bar{D}}_n}{\bar{D}_n} \times 100 \quad (7b)$$

$$J_D = \frac{1}{R}\left(\sum_{r=1}^{R}\left[1 - \frac{\hat{\bar{D}}_{DLS}(\theta_r)}{\bar{D}_{DLS}(\theta_r)}\right]^2\right)^{0.5}, \quad (7c)$$

where $\hat{\bar{D}}_n$ is the estimate of the number-average diameter, $\bar{D}_n$. Any mean diameter $\bar{D}_{a,b}$, can be calculated from:

$$\bar{D}_{a,b} = \left[\frac{\sum_{i=1}^{N} f(D_i) D_i^a}{\sum_{i=1}^{N} f(D_i) D_i^b}\right]^{\frac{1}{a-b}}; \qquad a, b = 1, 2, 3, ...; (a > b) \quad (8)$$

in particular, $\bar{D}_n$=$\bar{D}_{1,0}$ and the weight-average mean diameter $\bar{D}_w$=$\bar{D}_{4,3}$.

Note that in a real measurements, it would be impossible to calculate J_f and E_D. However, these criteria were adopted here to investigate the limitations of the proposed methodology. In Table 1, the true and estimated values of $\bar{D}_{1,0}$, $\bar{D}_{4,3}$, $\bar{D}_{6,5}$, and the resulting performance indexes obtained for NN and TR estimates of the 3 PSDs are presented. As expected, the recovery of the highly skewed $f_2(D_i)$ (see Figure 3a) was poorer than in the case of $f_1(D_i)$ and $f_3(D_i)$ (Figures 2a, 4a). For $f_1(D_i)$, the NN method produced better estimates than the TR, while for $f_2(D_i)$ and $f_3(D_i)$, both the NN and TR produced similar results. The TR method produced a good recovery of the PSD and its measured mean diameters only for the relatively broad $f_3(D_i)$.

5 NN Based Model Test with Experimental Data

The NN was experimentally tested through the MDLS measurements of two PS latexes (L1 and L2), of unknown PSDs $f_4(D_i)$ and $f_5(D_i)$, respectively. Latex L1 was a narrow standard (from Duke Scientific) with a nominal diameter of $1.11 \cdot 10^{-7}$ m (111 nm). Latex L2 was synthesized at POLYMAT laboratories with a nominal diameter of $2.00 \cdot 10^{-7}$ m (200 nm). For MDLS measurements, a general purpose laser light-scattering photometer (from Brookhaven Instruments Corporation) was fit with a vertically-polarized He-Ne laser ($\lambda = 6.328 \cdot 10^{-7}$ m (632.8 nm)) and a digital correlator (model BI-2000 AT). The measurements were carried out at 30 °C (T = 303.15 K), and at 13 different detection angles from 20° to 140°, at regular intervals of 10°. The total measuring times ranged from 200 to 500 s. The PS latexes were well diluted in distilled and deionized water to avoid multiple scattering, yielding mean intensities lower than 200.000 counts/s [27].

The 'measured' DLS average diameters, $\bar{D}_{DLS,meas.}(\theta_r)$, were calculated from the set of measured autocorrelation functions through the quadratic cumulants method [29] and are indicated by dots in Figures 6a and 7a.

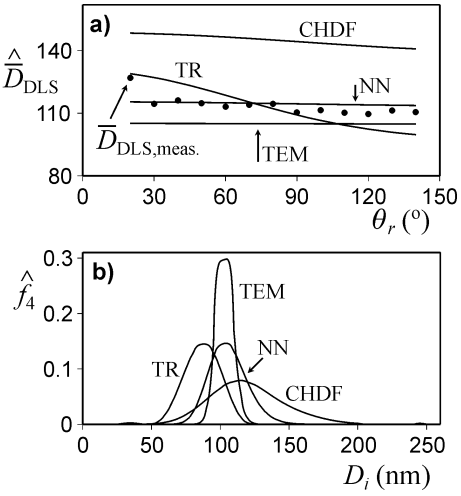

Fig. 6: Experimental example: PS standard L1, $f_4(D_i)$. a) Average DLS diameters, $\bar{D}_{DLS,meas.}(\theta_r)$, calculated by cumulants [29] (dots), and their simulated values from the estimated PSDs. b) Comparison of the PSDs measured by TEM and CHDF with the PSDs estimated through the NN and TR techniques.

Table 1: Simulated examples. True and estimated mean diameters, and performance indexes for the estimated PSDs.

	Log-normal PSD: $f_1(D_i)$			EMG PSD: $f_2(D_i)$			Gaussian PSD: $f_3(D_i)$		
	True	Estimates by:		True	Estimates by:		True	Estimates by:	
		NN	TR		NN	TR		NN	TR
$10^9 \times \bar{D}_{1,0}$ (m)[(a)]	204.2	205.9	189.5	360.0	365.4	355.4	450.0	451.7	448.4
$10^9 \times \bar{D}_{4,3}$ (m)[(a)]	212.5	211.6	206.3	364.4	368.2	362.1	461.7	462.7	461.2
$10^9 \times \bar{D}_{6,5}$ (m)[(a)]	218.2	215.4	215.2	368.0	370.0	366.4	469.2	470.1	469.3
J_f (–)[(b)]	–	0.189	0.415	–	0.430	0.421	–	0.062	0.095
E_D (%)[(c)]	–	–0.83	7.20	–	–1.50	1.28	–	–0.38	0.36
J_D (–)[(d)]	–	0.0021	0.0065	–	0.0038	0.0076	–	0.0022	0.0019

[(a)]Eq. (8); [(b)]Eq. (7a); [(c)]Eq. (7b); [(d)]Eq. (7d)

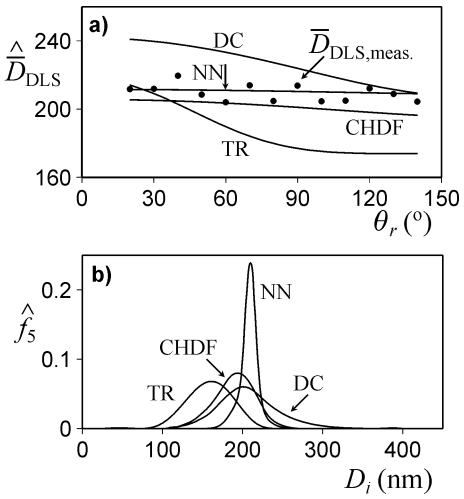

Fig. 7: Experimental example: PS latex L2, $f_5(D_i)$. a) Average DLS diameters, $\bar{D}_{DLS,meas.}(\theta_r)$, calculated by cumulants [29] (dots), and their simulated values from the estimated PSDs. b) Comparison of the PSDs measured by CHDF and DC with the PSDs estimated through NN and TR techniques.

These values were fed into the proposed NN, and the resulting estimated PSDs are represented in Figures 6b and 7b. For comparison, the same regularization technique used in the simulated examples was now applied to the autocorrelation functions obtained for latexes L1 and L2. The estimated PSDs are indicated by 'TR' in Figures 6b and 7b.

The latex L1 was also characterized by TEM and CHDF (see Figure 6b), while the latex L2 was measured by DC and CHDF (Figure 7b). For TEM measurements, the diluted latex was placed on a grid, dried overnight and Hitachi H-7000 FA equipment was used. The image analysis software BOLERO (Universidad de Granada, Spain) was used to compute the PSD after counting about 500 particles. For CHDF, a Matec Applied Sciences instrument was used at the following experimental conditions: flow-rate $2.33 \cdot 10^{-5}$ L/s, temperature 308.15 K, sample concentration < 0.5 wt% and carrier fluid 2X-GR500 (from Matec). Particle detection was accomplished by means of a sensitive UV detector at a fixed wavelength of $2.20 \cdot 10^{-7}$ m (220 nm). For DC, a BI-DCP (from Brookhaven Instrument Corporation) equipment was used at 9000 rpm and 35 °C. A mixture of dodecane/methanol/water (1/2/150 by volume) was employed as the spin fluid (viscosity = 0.955 cP, density = 0.998 kg/L). The latex samples were diluted to a concentration lower than 0.5 vol% in the same spin fluid.

The obtained PSDs were used to simulate the measurements of the DLS mean diameters on the basis of Eq. (2) yielding the curves $\hat{\bar{D}}_{DLS}(\theta_r)$ indicated in Figures 6a and 7a. Note that the relatively high mean diameters predicted by the TR technique at low angles fit with the presence of small peaks in the PSDs near $2.50 \cdot 10^{-7}$ m (250 nm) for L1 and $4.00 \cdot 10^{-7}$ m (400 nm) for L2, which are almost imperceptible in Figures 6b and 7b. In Table 2, the mean diameters $\bar{D}_{1,0}$, $\bar{D}_{4,3}$, and $\bar{D}_{6,5}$ (Eq. (8)) and the performance indexes (Eq. (7)) corresponding to latex L1 are presented. For L1, the TEM measurement was assumed to be an accurate approximation of the true PSD (even though it is known that TEM can underestimate the polydispersity or make biased estimates [5]). The NN method produced the best PSD estimate (see Figure 6b) and consequently lower performance indexes than the other techniques (see Table 2). For L2, the NN method produced the narrowest PSD estimate (Figure 7a) and from such PSDs, the $\hat{\bar{D}}_{DLS}(\theta_r)$ predictions were close to the measured DLS diameters (Figure 7a). In Table 3, the mean diameters and the J_D performance index (Eq. (7c)) are presented (the other performance indexes cannot be evaluated because a 'true' PSD was unavailable for L2). The minimum J_D corresponded to the PSD obtained through the NN estimation method.

Table 2: Experimental example (PS standard L1, 111 nm.). Estimated mean diameters, and performance indexes. Comparison with TEM, CHDF, and TR techniques.

	Estimates of $f_4(D_i)$ by:			
	TEM	CHDF	TR	NN
$10^9 \times \bar{D}_{1,0}$ (m)[(a)]	103.1	119.4	87.11	105.6
$10^9 \times \bar{D}_{4,3}$ (m)[(a)]	104.3	136.2	98.09	111.3
$10^9 \times \bar{D}_{6,5}$ (m)[(a)]	105.0	146.3	127.4	115.2
J_f (-)[(b)]	–	0.798	0.881	0.529
E_D (%)[(c)]	–	–15.8	15.5	–2.43
J_D (–)[(d)]	–	0.106	0.0338	0.0255

[(a)]Eq. (8); [(b)]Eq. (7a); [(c)]Eq. (7b); [(d)]Eq. (7c).

Table 3: Experimental example (PS latex L2, 200 nm.). Estimated mean diameters, and performance indexes. Comparison with TEM, CHDF, and TR techniques.

	Estimates of $f_5(D_i)$ by:			
	DC	CHDF	TR	NN
$10^9 \times \bar{D}_{1,0}$ (m)[(a)]	206.8	190.3	159.2	208.3
$10^9 \times \bar{D}_{4,3}$[(a)]	227.1	199.9	181.1	210.2
$10^9 \times \bar{D}_{6,5}$ (m)[(a)]	241.1	205.4	215.5	211.5
J_D (–)[(b)]	0.0255	0.0120	0.0348	0.0059

[(a)]Eq. (8); [(b)]Eq. (7c)

6 Conclusions

A method for estimating unimodal PSDs of polymer latexes from MDLS measurements was developed. The proposed method utilized a GRNN as an alternative to

solving an ill-conditioned non-linear inverse problem. The inputs to the NN were a few DLS average diameters, thus strongly reducing the extent of the problem that one would obtain if complete autocorrelation functions were employed. The NN was trained on the basis of simulated log-normal PSDs, with particles in a broad diameter range that covers most latexes of industrial interest.

The proposed method was successfully evaluated on the basis of synthetic and experimental examples. The trained NN was able to adequately recover PSDs of log-normal, EMG and Gaussian shapes. For the narrow PS standard, the PSD estimated through the NN method was better than that obtained from CHDF measurement. In all analyzed examples, the NN method predicted PSDs similar to or better than those obtained through classical inversion methods of MDLS measurements. From a practical point of view, the training of the NN was relatively simple and once the trained NN is available, the method presents the following advantages: i) it is a simple, fast and robust tool, ii) no specific method for numerical inversion is required and iii) no parameter adjustment is necessary, thus allowing the development of an automatic estimation procedure. Even though not shown, the NN also proved to be insensitive to standard measurement noises.

The proposed GRNN adequately predicted the most difficult case of estimating a narrow PSD, where the inversion of the MDLS measurements may produce small spurious peaks at both sides of the main PSD peak. For this reason, the NN approach could be applied for improving the quality of distributions obtained through fractionation techniques (e.g., CHDF with simultaneous detection of T and MDLS). In such cases, at each elution time, the NN could be used for estimating the PSD of each eluted fraction from MDLS and the T measurement could be used to obtain a better estimation of the particle number. Thus, no diameter calibration would be required.

Finally, the main limitation of the developed NN was that it was trained with only unimodal PSDs in a fixed diameter range and therefore, only unimodal PSDs in such ranges can be predicted. However, the NN ability can be extended to more general cases by augmenting the set of training PSDs (e.g., to include other distribution shapes or multimodal PSDs), by reducing the discretization diameter interval and/or by modifying the selection of the measurement angles.

7 Acknowledgment

The authors are grateful for financial support received from CONICET, MinCyT, Universidad Nacional del Litoral, and Universidad Tecnológica Nacional (Argentina). Financial support from the University of the Basque Country (UPV 221.215-13594/2001) and Ministerio de Educación y Ciencia (CTQ2006-03412/PPQ) is also greatly appreciated.

8 Nomenclature

Symbols

A	–	adjustable constant for modeling noisy measurements (Eq. (6))
C_I	–	fraction of light intensity scattered by a particle of diameter D_i at θ_r
$\mathbf{c}_k$	m	($R \times 1$ vector) center of the k-th neuron in a RFB NN
D_0	m	particle diameter of a monodisperse PSD
$\bar{D}_{a,b}$	m	average particle diameter ($a > b$) (Eq. (8))
$\bar{D}_{\mathrm{DLS}}$	m	average particle diameter obtained from DLS measurements
$\bar{\bar{D}}_{\mathrm{DLS}}$	m	mean value of $\bar{D}_{\mathrm{DLS}}(\theta_r)$
$\mathbf{D_{DLS}}$	m	($R \times 1$ vector) average diameters derived from DLS measurements
$\mathbf{D}^p_{\mathbf{DLS}}$	m	($R \times 1$ vector) average diameters used for NN training
$\bar{D}_{\mathrm{G}}$	m	mean diameter of a Gaussian PSD
$\bar{D}_g$	m	geometric mean diameter of a log-normal PSD
D_i	m	particle diameters of a PSD
$D_{\min}$, $D_{\max}$	m	minimum and maximum values of the discrete diameter axis
$\bar{D}_n$	m	number-average particle diameter ($= \bar{D}_{1,0}$)
$\bar{D}_w$	m	weight-average particle diameter ($= \bar{D}_{4,3}$)
E_D	–	performance index for the estimates of $\bar{D}_n$ (Eq. (7b))
f	–	number-fraction of particles (in an arbitrary PSD)
f_j	–	number PSD corresponding to the j-th example ($j = 1, ..., 5$)
$\mathbf{f}$	–	($N \times 1$ vector) number of particles
$\mathbf{f}^p$	–	($N \times 1$ vector) number of particles (target for the NN training)
$G^{(2)}_{\infty,\theta_r}$	–	baseline of the second-order autocorrelation function (at θ_r)
$G^{(2)}_{\theta_r}$	–	ordinates of the second-order autocorrelation function of the scattered light (at θ_r)
$g^{(1)}_{\theta_r}$	–	ordinates of the first-order autocorrelation function of the electric field (at θ_r)

h_k	–	output of the k-th hidden neuron
J_D	–	performance index for the estimates of $\bar{D}_{\mathrm{DLS}}(\theta_r)$ (Eq. (7c))
J_f	–	performance index for the estimates of the PSDs (Eq. (7a))
K	–	total number of hidden neurons in a RBF NN
k_{B}	J/K	Boltzmann constant ($= 1.38 \cdot 10^{-23}$ J/K)
k_{θ_r}	–	constants for DLS measurements (Eq. (1b))
M	–	number of points of the autocorrelation functions
N	–	number of points of the PSD
n_m	–	refractive index of the non-absorbing medium
n_p	–	particle refractive index
P	–	number of input/output pairs used in the NN training ($P = K$ for a GRNN)
R	–	number of DLS measurement angles
T	K	absolute temperature
w_{ik}	–	hidden-to-output weight factor of the NN
β	–	instrumental parameter for the DLS measurements (Eq. (1a))
Γ_0	m/s	θ_r-dependent parameter for DLS measurements (Eq. (1c))
ΔD	m	diameter interval of the discrete number PSD
ε	–	Gaussian random sequence of mean zero and variance one (Eq. (6))
η	Pa S	dynamic medium viscosity
θ_r	°	detection angle in MDLS measurements
λ	m	in vacuo laser wavelength
σ_{L}	–	standard deviation of a log-normal PSD
σ_{G}	m	standard deviation of a Gaussian PSD
$\sigma_{s,k}$	m	smoothing parameter (or 'spread') of the k-th hidden neuron
τ	m	decay constant of a decreasing exponential function
τ_j	s	discrete time delay of the autocorrelation function
$\hat{}$		indicates estimated value
$\tilde{}$		indicates measurement contaminated by noise
$*$		indicates convolution product
$^{\mathrm{T}}$		indicates transposed vector

Abbreviations

CHDF	capillary hydrodynamic fractionation
DC	disc centrifugation
DLS	dynamic light scattering
ELS	elastic light scattering
EMG	exponentially-modified Gaussian
ESEM	environmental scanning electron microscopy
GRNN	general regression neural network
MDLS	multiangle dynamic light scattering
NN	neural network
PS	polystyrene
PSD	particle size distribution
RBF	radial basis function
STEM	scanning transmission electron microscopy
T	turbidimetry
TEM	transmission electron microscopy
TR	Tikhonov regularization

9 References

[1] R. G. Gilbert, *Emulsion Polymerization. A Mechanistic Approach*. Academic Press, London, **1995**.

[2] M. Barandiaran, J. C. de la Cal, J. M. Asua, Emulsion Polymerization, in *Polymer Reaction Engineering* (Ed.: J. M. Asua), Blackwell Pub, Oxford, **2007**, pp. 233–272.

[3] T. Kourti, *Polymer Latexes Production by Homogeneous Nucleation and Methods for Particle Size Determination*, PhD Thesis, McMaster University, Canada, **1989**.

[4] M. A. Llosent, L. M. Gugliotta, G. R. Meira, Particle Size Distribution of SBR and NBR Latexes by UV-Vis Turbidimetry Near the Rayleigh Region. *Rubb. Chem. Technol.* **1996**, *69*, 696–712.

[5] H. J. Schöpe, O. Marnette, W. van Megen, G. Bryant, Preparation and Characterization of Particles with Small Differences in Polydispersity. *Langmuir* **2007**, *23*, 11534–11539.

[6] A. Bogner, G. Thollet, D. Basset, P. H. Jouneau, C. Gauthier, Wet STEM: A New Development in Environmental SEM for Imaging Nano-objects Included in a Liquid Phase. *Ultramicroscopy* **2005**, *104*, 290–301.

[7] A. Bogner, P. H. Jouneau, G. Thollet, D. Basset, C. Gauthier, A History of Scanning Electron Microscopy Developments: Towards "Wet–STEM" Imaging. *Micron* **2007**, *38*, 390–401.

[8] M. Do Amaral, A. Bogner, C. Gauthier, G. Thollet, P. H. Jouneau, J. Y. Cavaille, J. M. Asua, Novel Experimental Technique for the Determination of Monomer Droplet Size in Miniemulsion. *Macromol. Rapid. Commun.* **2005**, *26*, 365.

[9] C. A. Silebi, J. G. Dos Ramos, Axial Dispersion of Submicron Particles in Capillary Hydrodynamic Fractionation. *AIChE J.* **1989**, *35*, 1351–1364.

[10] O. Elizalde, G. P. Leal, J. R. Leiza, Particle Size Distribution Measurements of Polymeric Dispersions: A Comparative Study. *Part. & Part. Syst. Charact.* **2000**, *17*, 236–243.

[11] E. M. Verdurmen, J. G. Albers, A. L. German, Polybutadiene latex particle size distribution analysis utilizing a disk centrifuge. *Colloid Polym. Sci.* **1994**, *272*, 57–63.

[12] C. F. Bohren, D. H. Huffman, *Absorption and Scattering of Light by Small Particles*. John Wiley & Sons, New York, **1983**.

[13] R. Pecora, *Dynamic Light Scattering. Applications of Photon Correlation Spectroscopy*. Plenum Press, New York, **1985**.

[14] B. Chu, *Laser Light Scattering*. Academic Press, New York, **1991**.

[15] O. Glatter, M. Hofer, C. Jorde, W. Eigner, Interpretation of Elastic Light-Scattering Data in Real Space. *J. Colloid Interface Sci.* **1985**, *105*, 577–586.

[16] R. Finsy, L. Deriemaeker, E. Geladé, J. Joosten, Inversion of Static Light Scattering Measurements for Particle Size Distributions. *J. Colloid Interface Sci.* **1992**, *153*, 337–354.

[17] L. M. Gugliotta, J. R. Vega, G. R. Meira, Latex Particle Size Distribution by Dynamic Light Scattering: Computer Evaluation of Two Alternative Calculation Paths. *J Colloid Interface Sci.* **2000**, *228*, 14–17.

[18] F. Scheffold, A. Shalkevich, R. Vavrin, J. Crassous, P. Schurtenberger, PCS Particle Sizing in Turbid Suspensions: Scope and Limitations, in *Particle Sizing and Characterization* (Eds.: T. Provder and J. Texter), ACS Symposium Series 881, American Chemical Society, Washington D. C., **2004**, pp. 3–32.

[19] R. S. Stock, W. H. Ray, Interpretation of Photon Correlation Spectroscopy Data: A Comparison of Analysis Methods. *J. Polym. Sci., Part B: Polym. Phys.* **1994**, *23*, 1393–1447.

[20] G. Eliçabe, G. Frontini, Determination of the Particle Size Distribution of Latex Using a Combination of Elastic Light Scattering and Turbidimetry: A Simulation Study. *J. Colloid Interface Sci.* **1996**, *181*, 669–672.

[21] G. Frontini, G. Eliçabe, A Novel Methodology to Estimate the Particle Size Distribution of Latex Using Relative Measurements of Elastic Light Scattering and Turbidimetry: A Simulation Study. *J. Chemom.* **2000**, *14*, 51–61.

[22] J. R. Vega, G. L. Frontini, L. M. Gugliotta, G. E. Eliçabe, Particle Size Distribution by Combined Elastic Light Scattering and Turbidity Measurements. A Novel Method to Estimate the Required Normalization Factor. *Part. Part. Syst. Charact.* **2003**, *20*, 361–369.

[23] P. G. Cummins, E. J. Staples, Particle Size Distributions Determined by a Multiangle Analysis of Photon Correlation Spectroscopy Data. *Langmuir* **1987**, *3*, 1109–1113.

[24] S. E. Bott, Enhanced Resolution Particle Size Distributions by Multiple Angle Photon Correlation Spectroscopy, in *Particle Size Analysis* (Ed.: P. J. Lloyd), J. Wiley & Sons, Washington D. C., **1988**, pp. 77–88.

[25] G. Bryant, J. Thomas, Improved Particle Size Distribution Measurements Using Multiangle Dynamic Light Scattering. *Langmuir* **1995**, *11*, 2480–2485.

[26] G. Bryant, C. Abeynayake, J. Thomas, Improved Particle Size Distribution Measurements Using Multiangle Dynamic Light Scattering. 2. Refinements and Applications. *Langmuir* **1996**, *12*, 6224–6228.

[27] J. R. Vega, L. M. Gugliotta, V. D. Gonzalez, G. R. Meira, Latex Particle Size Distribution by Dynamic Light Scattering. A Novel Data Processing for Multi-angle Measurements. *J. Colloid Interface Sci.* **2003**, *261*, 74–81.

[28] V. D. Gonzalez, L. M. Gugliotta, J. R. Vega, G. R. Meira, Contamination by Larger Particles of Two Almost-Uniform Latexes: Analysis by Combined Dynamic Light Scattering and Turbidimetry. *J. Colloid Interface Sci.* **2005**, *285(2)*, 581–589.

[29] D. E. Koppel, Analysis of Macromolecular Polydispersity in Intensity Correlation Spectroscopy: The Method of Cumulants. *J. Chem. Phys.* **1972**, *57*, 4814–4820.

[30] A. N. Tikhonov, V. Arsenin, *Solution of Ill-posed Problems*. Wiley, New York, **1977**.

[31] A. Kirsch, *Introduction to the Mathematical Theory of Inverse Problems*. Springer-Verlag, New York, **1996**.

[32] H. W. Engl, M. Hanke, A. Neubauer, *Regularization of Inverse Problems*. Kluwer Academic Publishers, Dordrecht, The Netherlands, **1996**.

[33] P. C. Hansen, D. P. O'Leary, The Use of the L-curve in the Regularization of Discrete Ill-posed Problems. *SIAM J. Sci. Comput.* **1993**, *14*, 1487–1503.

[34] S. W. Provencher, A Constrained Regularization Method for Inverting Data Represented by Linear Algebraic or Integral Equations. *Comput. Phys. Commun.* **1982**, *27*, 213–227.

[35] S. W. Provencher, CONTIN: A General Purpose Constrained Regularization Program for Inverting Noisy Linear Algebraic and Integral Equations. *Comput. Phys. Commun.* **1982**, *27*, 229–242.

[36] P. C. Hansen, Regularization Tools: A Matlab Package for Analysis and Solution of Discrete Ill-posed Problems. *Numerical Algorithms* **1994**, *6*, 1–35.

[37] P. N. Pusey, W. van Megen, Detection of Small Polydispersities by Photon Correlation Spectroscopy. *J. Chem. Phys.* **1984**, *80(8)*, 3513–3520.

[38] G. Bryant, S. Martin, A. Budi, W. van Megen, Accurate Measurement of Small Polydispersities in Colloidal Suspensions. *Langmuir* **2003**, *19*, 616–621.

[39] Z. Ulanowski, Z. Wang, P. Kaye, I. Ludlow, Application of neural networks to the inverse light scattering problem for spheres. *Appl. Optics* **1998**, *37(18)*, 4027–4033.

[40] M. Li, T. Frette, D. Wilkinson, Particle Size Distribution Determination from Spectral Extinction Using Neural Networks. *Ind. Eng. Chem. Res.* **2001**, *40*, 4615–4622.

[41] R. Guardani, C. A. O. Nascimento, R. S. Onimaru, Use of Neural Networks in the Analysis of Particle Size Distribution by Laser Diffraction: Tests with Different Particle Systems. *Powder Technol.* **2002**, *126*, 42–50.

[42] V. V. Berdnik, R. D. Mukhamedyarov, V. A. Loiko, Sizing of Soft Spheroidal Particles by Multiangle Scattered Light Intensity Data: Applications of Neural Networks. *J. Quant. Spectr. Rad. Transfer* **2004**, *89*, 279–289.

[43] V. V. Berdnik, V. A. Loiko, Sizing of Spheroidal and Cylindrical Particles in a Binary Mixture by Measurement of Scattered Light Intensity: Applications of Neural Networks. *J. Quant. Spectr. Rad. Transfer* **2005**, *91*, 1–10.

[44] L. Deriemaeker, R. Finsy, Shape and Size Determination by Laser Diffraction: Average Aspect Ratio and Size Distribution by Volume; Feasibility of Data Analysis by Neural Networks. *Part. Part. Syst. Charact.* **2005**, *22*, 5–13.

[45] D. F. Specht, The General Regression Neural Network-Rediscovered. *Neural Networks* **1993**, *6(7)*, 1033–1034.

[46] S. Haykin, *Neural Networks: A Comprehensive Foundation*, 2nd ed. Englewood Cliffs, NJ: Prentice Hall, **1999**.

[47] P. D. Wasserman, *Advanced Methods in Neural Computing*. Van Nostrand Reinhold, New York, **1993**.

[48] T. Inagaki, E. T. Arakawa, R. N. Hamm, M. W. Williams, Optical Properties of Polystyrene from the Near Infrared to the X-Ray Region and Convergence of Optical Sum Rules. *Phys. Rev. B* **1977**, *15*, 3243–3253.

[49] M. Kerker, *The Scattering of Light and Other Electro-Magnetic Radiation*. Academic Press, New York, **1969**.

